Fast Dual Trifeature-Based Detection of Small Targets in Sea Clutter by Using Median Normalized Doppler Amplitude Spectra

Zi-Xun Guo [ID], Xiao-Hui Bai [ID], Peng-Lang Shui [ID], *Senior Member, IEEE*, Ling Wang, and Jia Su, *Member, IEEE*

Abstract—High-resolution sea-surface surveillance radars are designed to find two classes of small targets, low-velocity and floating small targets on the sea surface and low-altitude small targets over the sea surface. Existing feature-based detectors using amplitude and Doppler spectra features of returns can fast detect the first class of small targets. But they often fail to find the second class of small targets due to their small radar cross-sections and low signal-to-clutter ratios (SCR). This article proposes a fast dual trifeature-based detector to find the two classes of small targets. At the low-velocity trifeature-based detector, the existing trifeature-based detector is used to find the first class of small targets. At the high-velocity trifeature-based detector, a new trifeature-based detector is used to detect the second class of small targets by utilizing three new features from the median normalized Doppler amplitude spectrum (MNDAS). Owing to the ability of the MNDAS to suppress sea clutter, the high-velocity trifeature-based detector can effectively find the second class of small targets with low SCRs. The detected results in the two trifeature-based detectors are combined into the binary output of the detector in terms of the "OR" operation. Finally, the proposed detector is verified and compared with the existing detectors by the open and recognized IPIX and CSIR radar databases and one unmanned aerial vehicle radar dataset. Besides the detection performance for the two classes of small targets, a merit of the proposed detector is of low-complexity decision because no time-frequency features are available in detection.

Index Terms—Fast dual trifeature-based detector, low-altitude small targets, low-velocity and floating small targets, median normalized Doppler amplitude spectra (MNDAS), sea clutter.

I. INTRODUCTION

IT IS an important and difficult task for high-resolution maritime surveillance radars to detect two classes of small targets, low-velocity and floating small targets on the sea surface and low-altitude small targets over the sea surface. Small targets include small boats, icebergs, periscopes of submarines, low-altitude unmanned aerial vehicles (UAVs), and so on. The difficulties in detecting them come from three aspects. First, sea clutter time sequences with strong non-Gaussianity are difficult to be modeled in an observation time of the order of subsecond or seconds in simple formats [1], [2]. Second, small targets have weaker radar returns than sea clutter because of their small radar cross-sections (RCS). Third, complex interactions of the first class of small targets and maneuvering flight of the second class of small targets make it difficult to parametrically model their radar returns in a long observation time [3].

Early, incoherent detection methods are usually used to detect small targets in sea clutter, such as the cell-average constant false alarm rate (CA-CFAR) detector, the greatest/smallest of CFAR detector [4]. In coherent radar systems, the adaptive detection methods are based on statistical models of sea clutter to develop a series of optimal or near-optimal detectors, such as the generalized likelihood ratio test (GLRT) [5], adaptive matched filter, and adaptive normalized matched filter (ANMF) detectors [6]. In addition to the commonly-used statistical distribution models of sea clutter, sea clutter time series can be modeled as a nonlinear dynamic system, and the characteristics of the system can be used to detect targets, like chaos theory and neural network [7]. However, when the observation time is up to several tenths of one second or the order of seconds, sea clutter time series have time-varying power, and target returns have unknown nonlinear Doppler offsets and amplitude modulations. Traditional adaptive detection methods fail to use because they often depend on parametric models of sea clutter and target returns. The feature-based detection, which does not depend on clutter statistical models and simple parametric models of target returns, is an effective approach for small target detection [8], [9], [10], [11], [12], [13], [14], [15], [16], [17], [18], [19], [20], [21], [22], [23].

Feature-based small target detection in sea clutter has constantly developed in succession along two approaches. One approach devotes to extracting features to improve performance [8], [9], [10], [11], [12], [13], [14], [15], [16], [17], [18], [19], [20], [21], [22], [23], and the other devotes to designing detectors to enhance performance and real-time implementation [14], [15], [16], [18], [19], [20], [21], [23], [24], [25], [26], [27], [28]. Both salient features and effective learning algorithms

Zi-Xun Guo is with the School of Electronics and Information, Northwestern Polytechnical University, Xi'an 710072, China, and also with the National Laboratory of Radar Signal Processing, Xidian University, Xi'an 710071, China (e-mail: zxguo_724@stu.xidian.edu.cn).

Xiao-Hui Bai and Peng-Lang Shui are with the National Laboratory of Radar Signal Processing, Xidian University, Xi'an 710071, China (e-mail: xhbai@stu.xidian.edu.cn; plshui@xidian.edu.cn).

Ling Wang and Jia Su are with the School of Electronics and Information, Northwestern Polytechnical University, Xi'an 710072, China (e-mail: lingwang@nwpu.edu.cn; jiasu1011@nwpu.edu.cn).

are indispensable. Different features are suitable for different cases [14], [15], and their complementarity is the base of the feature-based detectors with robust and good detection performance [26], [27]. Various learning algorithms [14], [15], [16], [17], [18], [19], [20], [21], [22], [23], [24], [25], [26], [27], [28] have been proposed to design decision functions, thresholds, or regions, including the convexhull learning algorithm [14], [15], [17], [22], [26], the graphs [18], [19], the concave hull learning algorithm [21], the support vector machine (SVM) [16], [20], [23], the principal component analysis (PCA) [24], the decision tree [25], the K-nearest neighbor (KNN) algorithm [27], and convolutional neural networks [28]. With the increasingly improving feature-based detectors to fully meet the performance demand of maritime surveillance radars, the fast decision to support real-time implementation becomes more critical. Two factors to limit the fast decision are feature extraction and the calculation of the decision functions, such as the complex calculations of the normalized time-frequency (TF) features [15] and high-dimensional distances in the KNN-based detector [27].

This article first proves the SCR-dependency of features, proposes a normalization method to realize the sea clutter suppression, then develops three Doppler features with detection capabilities in low SCR, and finally proposes a fast dual trifeature-based detection method to detect the two classes of small targets in sea clutter. At the low-velocity trifeature-based detector, the combination of the three features and convexhull decision is used to detect the first class of small targets on the sea surface. Due to the absence of clutter suppression in the three features, the low-velocity trifeature-based detector cannot find small targets with relatively high velocity and very small RCS. At the high-velocity trifeature-based detector, the median normalized Doppler amplitude spectrum (MNDAS) with low computational complexity is proposed for adaptive sea clutter suppression before feature extraction. From the MNDAS, three new features, the peak height (PH), the local accumulation (LA), and the vector entropy (VE), are extracted. The three new features combined with the convexhull decision to effectively detect the second class of small targets. Finally, the detection result is the "OR" fusion of the binary results at the two trifeature-based detectors. The proposed fast dual trifeature-based detector is verified by the two recognized IPIX and CSIR radar databases and one specific UAV dataset. The results show that it obtains the effective tradeoff between detection performance and computational costs.

The rest of this article is organized as follows. Section II briefly introduces two open radar databases and one specific dataset for small target detection in sea clutter. Section III gives the SCR-dependency verification and analysis of existing features and analyzes their limitations. Section IV, the MNDAS and three new salient features are proposed, and the dual trifeature-based detector is constructed. Section V reports the experimental results on the three databases and analyzes their computational costs. Finally, Section VI concludes this article.

II. DESCRIPTIONS OF OPEN AND SPECIFIC DATABASES

The two open IPIX and CSIR databases [29], [30] for small target detection in sea clutter and one special UAV radar

TABLE I
PARAMETERS OF THE IPIX DATABASE, CSIR DATABASE, AND UAV DATASET

Database	IPIX		CSIR	UAV dataset
	1993	1998		
Carrier frequency	9.39 GHz		9.0/6.5 GHz	10 GHz
PRF	1000 Hz		2500/5000 Hz	4000 Hz
Range resolution	30 m	30/15/9 m	15 m	3 m
Sea state	2/3/4	–	4	2
Polarization	HH/HV/VH/VV		VV	VV
Operating mode	Staring		Staring/tracking	Staring
Band	X		X/C	X
Test target	An anchored spherical block with a diameter of 1 m and wrapped in wires	Floating small boats	Motorized small boats	A M300 DJI UAV with four rotors and a corner reflector of eight trihedrons fixed on the back of the UAV
Average SCR	−1.5 dB ~ 18.3 dB	−3.6 dB ~ 28.5 dB	9.2 dB ~ 17.1 dB	−8.8 dB ~ −4.9 dB
Radial velocity	−0.8 m/s ~ 0.9 m/s		−5.8 m/s ~ 9.2 m/s	−15 m/s to 15 m/s

dataset from an island high-resolution radar are available for performance evaluation. Table I lists important information about the two open databases and the UAV dataset. Twenty datasets from the IPIX radar database include the ten datasets (labeled 17, 26, 30, 31, 40, 54, 280, 310, 311, and 320) collected in 1993 and the ten datasets (labeled 202225, 202525, 163113, 171437, 180558, 195704, 164055, 173317, 173950, and 184537) collected in 1998. In these datasets, the test floating small targets have small radial velocities and higher SCRs and fall into the main clutter region of sea clutter in the Doppler domain. The ten datasets from the CSIR radar database are the TFA10_004, TFA10_005, TFA10_006, TFA10_007, TFA10_008, TFA17_001, TFA17_002, TFA17_004, TFA17_005, and TFA17_006. The test targets are moving small boats, and their radar returns sometimes fall outside the main clutter region of sea clutter in the Doppler domain [27], [30].

The specific UAV dataset was collected by our team by an experimental radar mounted on a mountain top at an island, Qingdao, China. The height of the radar is about 450 m over the sea level. Fig. 1(a) illustrates the test target in the experiment. The average RCS is about 0.6 m^2, and the RCS of the UAV can be ignored compared with the corner reflector owing to the material of the UAV. In the experiment, the UAV was flying 50–100 m above sea level. Fig. 1(b) is the trace of the UAV flight path in the radar beam. Fig. 1(c) illustrates the power map of the radar returns of radial distance from 4.3 to 5.5 km during 300 s, corresponding to the trace indicated in the red ellipse of Fig. 1(b). The SCRs of the UAV returns are much less than 0 dB, thus its trace is invisible in the power map. The data of the first 38 s labeled by "Training region" are sea clutter and are used to train the feature-based detectors in the sequent experiments. The data outside the region are used to verify detectors in both
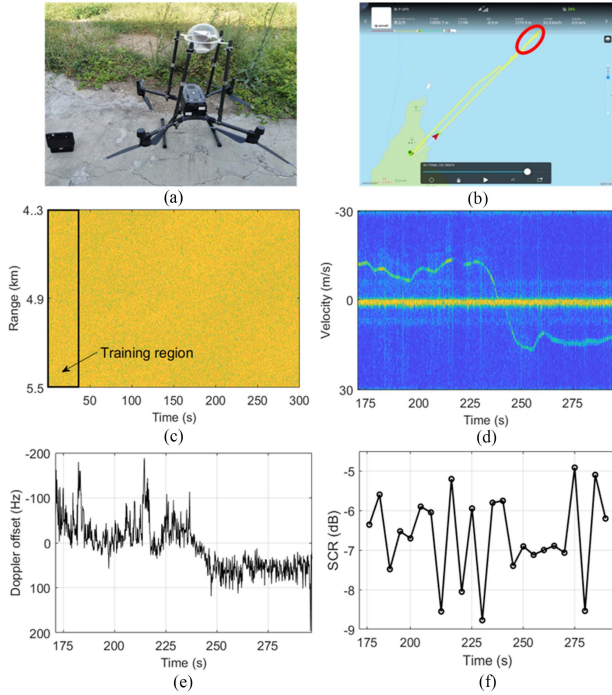
Fig. 1. Description of the special UAV dataset, (a) the test target, (b) the GPS trace of the UAV flight in the radar beam, (c) the power map of the radar returns, (d) the TFD of the radar returns along the UAV trace, (e) the Doppler offset of the target returns along the UAV trace, and (f) SCRs of the target returns.

detection probability and false alarm rate. Fig. 1(d) plots the TF distribution (TFD) of the radar returns along the UAV trace. Due to too low SCRs, the Doppler offset trace of the UAV can be hazily observed, where the yellow strip is from the sea clutter. Obviously, sea clutter is much stronger than the target returns. To further analyze the characteristics of the target returns, Fig. 1(e) plots the Doppler offset traces, where sea clutter is removed by a high-pass filter. The UAV's maneuvering flight results in the fluctuation of the radial velocity. Moreover, except around the farthest point, the target returns fall outside the main clutter domain of sea clutter in the Doppler domain. Fig. 1(f) plots the SCRs of the target returns along the UAV trace. Hence, the UAV dataset is suited to verify the performance of a detector on small targets with relatively high radial velocity.

III. SCR-DEPENDENCY VERIFICATION AND LIMITATION ANALYSIS OF FEATURES

When the observation time is long up to several tenths of a second, small target detection in sea clutter boils down to the following binary hypothesis [8], [9], [10], [11], [12], [13], [14], [15], [16], [17], [18], [19], [20], [21], [22], [23], [24], [25], [26], [27], [28]:

$$
\begin{cases}
H_0 : \begin{cases} z(n) = c(n), n = 1, 2, \dots N, \\ z_p(n) = c_p(n), p = 1, 2, \dots, P, \end{cases} \\
H_1 : \begin{cases} z(n) = s(n) + c(n), n = 1, 2, \dots N, \\ z_p(n) = c_p(n), p = 1, 2, \dots, P \end{cases}
\end{cases}
\tag{1}
$$

where N is the length of the time series, P is the number of the reference cells, H_0 is the null hypothesis, H_1 is the alternative hypothesis, $z(n)$ and $z_p(n)$ are complex radar returns time sequences at the cell under test (CUT) and P reference cells around the CUT, respectively. $c(n)$ and $c_p(n)$ are sea clutter time series at the CUT and reference cells, respectively. $s(n)$ are target returns, an unknown complex time series. For convenience in expressions, the sequences are denoted by the bold fonts $\mathbf{z}$ and $\mathbf{z}_p$. In all I features, the ith feature is the value of a nonlinear function Φ_i of the vectors $\mathbf{z}$ and $\mathbf{z}_p$ at the CUT and reference cells and is expressed in form by

$$
\xi_i = \Phi_i\left(\mathbf{z}, \mathbf{z}_1, \dots, \mathbf{z}_P\right), i = 1, 2, \dots, I.
\tag{2}
$$

Traditional adaptive detection concerns the statistics of the random variables in (2). Feature-based detection highlights the effectiveness and complementary of individual random variables in detection ability.

In feature-based detection of small targets in sea clutter, there have existed many salient features, including the normalized Hurst exponent (NHE) [10], the all-dimensional Hurst exponent (ADHE) [12], and the relative average amplitude (RAA) [14], which are calculated directly from radar returns; the relative Doppler peak height (RDPH) and the relative vector entropy (RVE) [14] calculated from the Doppler amplitude spectra; and the ridge integration (RI), the number of connected region (NR), and the maximal size of connected region (MS) [15] calculated from the TFD of radar returns.

Below, we analyze and prove the SCR-dependency of the fractal-based features, amplitude/intensity features, and two Doppler features. These features are all at low computational costs and can meet the demand of real-time target detection. The fractal-based features indicate the Hurst exponents of radar returns' amplitude, complex, and phase sequences at different time scales [12]. Taking the complex sequence as an example, the Hurst exponent H_{s+c} of sea clutter plus target returns is estimated by the power law

$$
r_{s+c}(m) = E\left\{|s(n+m) + c(n+m) - s(n) - c(n)|^2\right\}
$$
$$
\approx \left(\sigma_s^2 + \sigma_c^2\right)|m|^{2H_{s+c}}, 0 < m \leq \frac{T_{\text{speckle}}^{\text{decorr}}}{\Delta t}
\tag{3}
$$

where $\sigma_s{}^2$ and $\sigma_c{}^2$ are variances of the target returns and sea clutter, Δt is the pulse repetition interval (PRI) and $T_{\text{speckle}}^{\text{decorr}}$ is the decorrelated time of sea clutter. Then

$$
r_{s+c}(m) = r_s(m) + r_c(m) \approx \sigma_s^2|m|^{2H_s}
$$
$$
+ \sigma_c^2|m|^{2H_c}(1 \geq H_s > H_c > 0)
\tag{4}
$$

where H_s and H_c are the Hurst exponents of target returns and sea clutter, respectively. In terms of (3) and (4), when $SCR = \sigma_s^2/\sigma_c^2 \ll 1$ (low SCR cases)

$$
H_{s+c} - H_c \approx SCR \times \frac{|m|^{2(H_s - H_c)}}{2\log|m|}.
\tag{5}
$$

It means that the Hurst exponent difference of target returns plus sea clutter and sea clutter is *directly proportional to the SCR* when the scale range and the Hurst difference of target returns

and sea clutter are given. Therefore, the detection ability of the fractal-based features highly depends upon SCR, and the fractal-based features are ineffective in the case of low SCRs, for small differences at the Hurst exponents are difficult to distinguish target returns plus sea clutter from sea clutter.

The amplitude/intensity features are from the test statistics in the noncoherent integration at the linear detection and squared law detection [31]. Taking the squared law detection as an example, the average intensity of target returns plus sea clutter is given by

$$E\left((\mathbf{s}+\mathbf{c})^H(\mathbf{s}+\mathbf{c})\right) = E\left(\mathbf{s}^H\mathbf{s}\right) + E\left(\mathbf{c}^H\mathbf{c}\right)$$
$$= \sigma_s^2 + \sigma_c^2 = \sigma_c^2(1+SCR) \quad (6)$$

where $\mathbf{s}$ and $\mathbf{c}$ are the vectors of target and clutter time series, respectively. It means that the average intensity difference of target returns plus sea clutter is *directly proportional to the SCR*. Therefore, when the SCR is low, the average amplitude/intensity of the radar returns is difficult to distinguish the two-class returns. The detection ability of the average amplitude has a complicated relationship with SCR and similar results. Thus, the detection ability of the amplitude/intensity feature is sensitive to the SCR and will vanish in the cases of low SCR.

The RVE is a global feature of the Doppler amplitude/power spectrum (DAS/DPS) of the radar returns. It reflects the sparsity extent of the power distribution of the radar returns in the Doppler domain [14]. The VE of the power spectrum of target returns plus sea clutter is calculated by

$$VE(\mathbf{s}+\mathbf{c}) = \sum_k \frac{|S(k)+C(k)|^2}{\mathbf{s}^H\mathbf{s}+\mathbf{c}^H\mathbf{c}} \ln\left(\frac{\mathbf{s}^H\mathbf{s}+\mathbf{c}^H\mathbf{c}}{|S(k)+C(k)|^2}\right) \quad (7)$$

where $S(k)$ and $C(k)$ are the DFTs of the target returns $s(n)$ and sea clutter $c(n)$, respectively. When SCR is very low, $\mathbf{s}^H\mathbf{s}+\mathbf{c}^H\mathbf{c} \approx \mathbf{c}^H\mathbf{c}$, the difference between the two-class returns is approximated by

$$VE(\mathbf{c}) - VE(\mathbf{s}+\mathbf{c})$$
$$= \sum_k \left(\frac{|C(k)|^2}{\mathbf{c}^H\mathbf{c}}\ln\left(\frac{\mathbf{c}^H\mathbf{c}}{|C(k)|^2}\right) - \frac{|S(k)+C(k)|^2}{\mathbf{c}^H\mathbf{c}+\mathbf{s}^H\mathbf{s}}\right.$$
$$\left.\times \ln\left(\frac{\mathbf{c}^H\mathbf{c}+\mathbf{s}^H\mathbf{s}}{|S(k)+C(k)|^2}\right)\right)$$
$$\approx \sum_k \frac{|C(k)|^2}{\mathbf{c}^H\mathbf{c}}\ln\left(\frac{|S(k)+C(k)|^2}{|C(k)|^2}\right)$$
$$+ \sum_k\left(\frac{|S(k)+C(k)|^2 - |C(k)|^2}{\mathbf{c}^H\mathbf{c}+\mathbf{s}^H\mathbf{s}}\ln\left(\frac{\mathbf{c}^H\mathbf{c}+\mathbf{s}^H\mathbf{s}}{|S(k)+C(k)|^2}\right)\right)$$
$$\leq \sum_k \frac{|C(k)|^2}{\mathbf{c}^H\mathbf{c}}\ln\left(1+\frac{|S(k)|^2}{|C(k)|^2}\right)$$
$$+ \sum_k\left(\frac{|S(k)|^2}{\mathbf{c}^H\mathbf{c}+\mathbf{s}^H\mathbf{s}}\ln\left(\frac{\mathbf{c}^H\mathbf{c}+\mathbf{s}^H\mathbf{s}}{|S(k)+C(k)|^2}\right)\right)$$
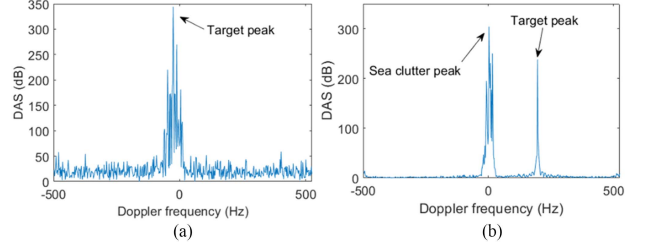

Fig. 2. DAS of two typical sequences of returns with targets, (a) floating target with high SCR from the IPIX radar database and (b) the high-velocity target with very low SCR from the UAV dataset.

$$\leq \frac{\mathbf{s}^H\mathbf{s}}{\mathbf{c}^H\mathbf{c}} + \frac{\mathbf{s}^H\mathbf{s}}{\mathbf{c}^H\mathbf{c}+\mathbf{s}^H\mathbf{s}}\max_k\left(\ln\left(\frac{\mathbf{c}^H\mathbf{c}+\mathbf{s}^H\mathbf{s}}{|S(k)|^2+|C(k)|^2}\right)\right)$$
$$\leq SCR\left(1+\max_k\left(\ln\left(\frac{\mathbf{c}^H\mathbf{c}+\mathbf{s}^H\mathbf{s}}{|S(k)|^2+|C(k)|^2}\right)\right)\right). \quad (8)$$

In terms of (8), the difference between the two-class returns in the power spectra' VE is *directly proportional to the SCR* and relevant to the power distributions of the target returns plus sea clutter on the Doppler domain. When the amplitude spectra are used, the situation is complex, and the result is similar. Thus, the RVE feature is difficult to distinguish between the two-class returns in the cases of low SCR.

It is known that the average Doppler spectra of sea clutter can be modeled by the bell-shaped functions, and the Doppler offsets and bandwidth depends on sea states, radar parameters, and the viewing geometry [1] (Chapter 2). The Doppler feature RDPH in [14] was extracted based on the fact that the Doppler amplitude spectra (DAS) of target returns have sharp peaks while the DAS of sea clutter have blunt peaks. In terms of the process to extract the RDPH in [14], the precondition of the RDPH to reflect the characteristics of target returns is that the maximal peak of the DAS of target return plus sea clutter is from target returns instead of sea clutter. However, when the SCR is very low, the Doppler peak of target returns is sometimes lower than that of sea clutter. Fig. 2 illustrates this phenomenon. Fig. 2 plots two DAS of target returns plus sea cutter in measured radar data. In the high SCR case as shown in Fig. 2(a), the Doppler peak of the target returns rides on the DAS of sea clutter and is higher than the maximum value of the DAS of sea clutter. Thus, the DPH reflects the sharpness of the Doppler peak of target returns. In the low SCR case as shown in Fig. 2(b), the Doppler peak locates outside the main clutter region of sea clutter and is lower than the maximum value of the DAS of sea clutter. In this case, the DPH reflects the sharpness of the Doppler peak of sea clutter instead of target returns. Therefore, the local Doppler feature RDPH sometimes fails to distinguish the two-class returns in the case of very low SCR.

We quantitatively examine the SCR-dependency of the detection abilities of individual features using measured radar datasets. Here, the 20 datasets at the four polarizations from the IPIX radar database are available. The average SCRs of the radar returns of the target under test are plotted in Fig. 3(a). To measure the detection ability of each feature on individual datasets, a detector using the feature as the test statistic is constructed
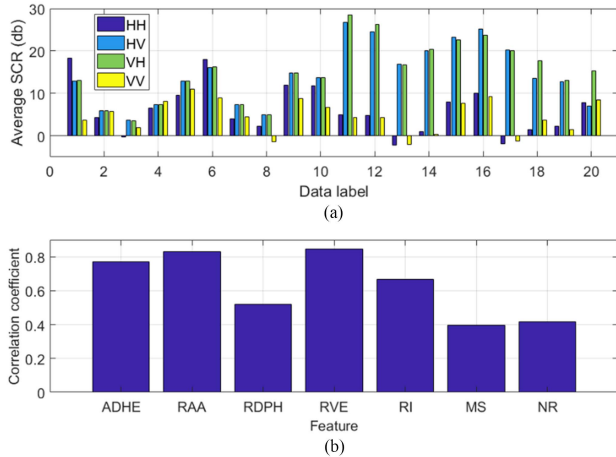
Fig. 3. Relation between detection performance of features and average SCR: (a) Average SCRs of the radar returns of the target under test, (b) correlation coefficients of the seven features between the average SCR and the detection probability.

as follows:

$$\xi_i = \Phi_i\left(\mathbf{z}, \mathbf{z}_1, \ldots, \mathbf{z}_P\right) \underset{<}{\overset{>}{}} T(P_F). \tag{9}$$

The decision threshold T at the false alarm rate P_F (0.001 in experiments) is obtained by the Monte-Carlo tests on sea clutter data of each dataset. The detection probability of the test target on the test set $\mathbf{S}_t$ is computed by

$$P_d \equiv \frac{\#\{\xi_i = \Phi_i(\mathbf{z}, \mathbf{z}_1, \ldots, \mathbf{z}_P) \underset{<}{\overset{>}{}} T(P_F), \mathbf{z} \in \mathbf{S}_t\}}{\#\{\mathbf{S}_t\}} \tag{10}$$

where $\#\{\mathbf{A}\}$ is the number of elements in the finite set $\mathbf{A}$. For some features, the alternative hypothesis holds as the ">" in (9) and (10) is satisfied, and the situation is converse for the RVE and NR. For each dataset, the detection ability of a feature at the average $\mathrm{SCR}(k)$ in decibels is measured by the detection probability $P_d(k)$. In this way, the SCR-dependency of the detection ability of the feature can be assessed by the correlation coefficient of the average SCR and the detection probability, i.e.,

$$\rho_i = \frac{\sum_{k=1}^{80}\left(SCR(k) - \overline{SCR}\right)\left(P_d(k) - \bar{P}_d\right)}{\sqrt{\sum_{k=1}^{80}\left(SCR(k) - \overline{SCR}\right)^2 \sum_{k=1}^{80}\left(P_d(k) - \bar{P}_d\right)^2}}, \tag{11}$$

$$\overline{SCR} = \frac{1}{80}\sum_{k=1}^{80} SCR(k), \bar{P}_d = \frac{1}{80}\sum_{k=1}^{80} P_d(k). $$

Fig. 3(b) plots the correlation coefficients of the seven features. It can be seen that all the correlation coefficients are positive, meaning that the detection ability of all seven features improves with the increase of the average SCR. However, the ADHE, RAA, and RVE have correlation coefficients over 0.75, and their detection abilities are sensitive to SCR, thus are difficult to find target returns of very low SCR. The NR and MS features have small correlation coefficients under 0.45, and thus their

detection abilities are insensitive to SCR, owing to the clutter suppression in feature extraction. The RDPH and RI features, respectively, have moderate correlation coefficients of 0.51 and 0.66. Through the analysis of Fig. 2, the RDPH's detection ability is highly related to the local SCR rather than the average SCR. In conclusion, the ADHE, RAA, RDPH, and RVE features do not have enough ability to detect small targets with very low SCRs and high radial velocities. It is necessary to construct new features of low computational complexities instead of the TF features of high computational complexities.

IV. FAST DUAL TRIFEATURE-BASED DETECTION METHOD

The traditional dual-channel adaptive detection scheme is widely used in practical radar systems [31] (Chapter 3, Section III-F), where the zero-velocity channel is used to find stationary and low-velocity targets by noncoherent integration, and the moving target detection channel via a Doppler filter bank is used to find moving targets by coherent integration and clutter suppression. The proposed method is a generalization of the dual scheme in feature-based detection where sea clutter and target returns are difficult to be parametrically modeled.

A. New Features From Median Normalized Doppler Spectra

In [35], the normalized DPS (NDPS) was proposed. The NDPS of the CUT is constructed by the DPS of the CUT time series subtracting the mean function and divided by the standard deviation function of the reference cell time series to adapt spatial-temporally varying characteristics of sea clutter. Similarly, in [15], the normalized time-frequency distribution (NTFD) was proposed. The NTFD of the CUT is constructed by the TFD of the CUT time series subtracting the mean function and divided by the standard deviation function of the reference cell time series. From the two detectors in [15] and [35], it is known that the normalization process can suppress sea clutter well. However, the mean normalization in [15] and [35] is not robust to outliers in reference cells. Here, the mean normalization is replaced by the median normalization to improve the robustness to outliers because the median, as an order statistic, is robust for a small number of outliers [36].

When small targets float on the sea surface and have interactions with sea waves, their radial velocities vary within a narrow range in a short time. The energy of returns with targets concentrates on a small number of Doppler bins. Whereas the energy of sea clutter spreads over a wide range of Doppler frequency, e.g., 100 to 150 Hz in terms of the IPIX database [14], [29]. For studying the differences between returns with targets and sea clutter in the Doppler domain, the DAS in the CUT and reference cells are computed as follows:

$$Z(f_d) = \frac{1}{\sqrt{N}}\left|\sum_{n=1}^{N} z(n)\exp(-2\pi f_d n T_r)\right|, -\frac{1}{2T_r} \le f_d \le \frac{1}{2T_r}$$

$$Z_p(f_d) = \frac{1}{\sqrt{N}}\left|\sum_{n=1}^{N} z_p(n)\exp(-2\pi f_d n T_r)\right|, -\frac{1}{2T_r} \le f_d \le \frac{1}{2T_r} \tag{12}$$
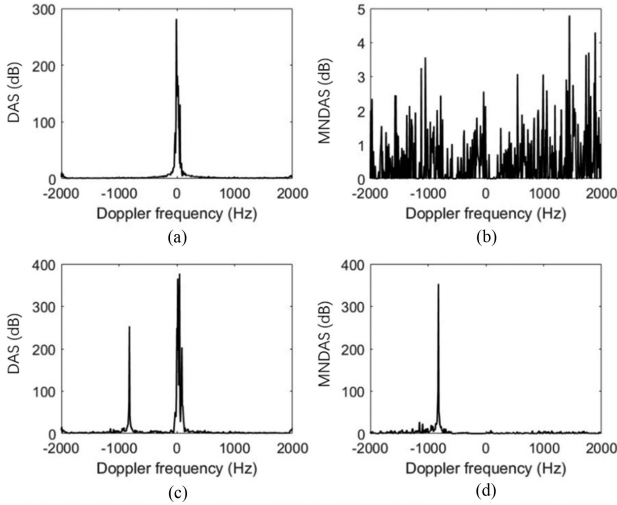
Fig. 4. Comparisons of two cases: (a) DAS of sea clutter, (b) MNDAS of sea clutter, (c) DAS of returns with targets, and (d) MNDAS of returns with targets.

where f_d is Doppler frequency, T_r is pulse repetition period of the radar. When the received radar returns contain targets, the DAS has a sharp peak; otherwise, the DAS has an obtuse peak [14]. However, in the case of low SCR, the Doppler peak of sea clutter is higher than that of returns with targets, and the target detection capability of the DAS will be degraded, such as the example in Fig. 2(b). To solve this problem and make detectors insensitive to SCR, we develop a normalization method based on the median and deviation median of the DAS for subsequent detection.

First, since the statistics of sea clutter are time- and space-varying, according to (1), the median and deviation median of the sea clutter DAS can be estimated from the sea clutter of P reference cells by the following (13) and (14), respectively,

$$\hat{Z}_c(f_d) = median\{Z_p(f_d), p = 1, 2, \ldots, P\}, \tag{13}$$

$$\hat{\sigma}_c(f_d) = median\{|Z_p(f_d) - \hat{Z}_c(f_d)|, p = 1, 2, \ldots, P\} \tag{14}$$

where the median$\{\cdot\}$ is the median operation. When outliers exist and are included in samples, the median is more stable than the mean [36]. Second, the MNDAS in the CUT can be expressed as follows:

$$Y(f_d) \equiv \frac{\max\{Z(f_d) - \hat{Z}_c(f_d), 0\}}{\hat{\sigma}_c(f_d)}. \tag{15}$$

According to the normalization method from (15), Fig. 4 shows the normalization of sea clutter and returns with targets, where (a) and (c), respectively, plot the DAS of sea clutter and returns with targets, (b) and (d), respectively, plot the MNDAS of sea clutter and returns with targets. It can be found that the MNDAS of sea clutter lose the peak and decrease the clutter level in contrast with the DAS of sea clutter. The normalization method can effectively suppress sea clutter in the Doppler domain. Unlike the MNDAS of sea clutter, the MNDAS of returns with targets remain and enhance the sharp peak about the target while simultaneously suppressing sea clutter around the zero frequency. This merit from the MNDAS will benefit the proposed detector.

B. Extractions of Three New Features Based on MNDAS

The existing features in the previous trifeature-based detector [14] are mainly used to detect low-velocity and floating small targets on the sea surface, like floating spherical blocks and floating small boats of the IPIX databases [29]. The previous trifeature-based detector based on the DAS does not have sea clutter suppression, and its detection capability heavily depends on SCR. Unlike the DAS, the proposed MNDAS suppress sea clutter and are more suitable for detecting targets under low SCR.

By observing Fig. 4(b) and (d), the MNDAS power of returns with targets concentrates on several Doppler bins and has a sharp peak, whereas the MNDAS power of sea clutter is widely distributed in the Doppler bins. Returns with targets have larger peak values than sea clutter. So, the first extracted feature is the PH of the MNDAS and can be expressed as follows:

$$\text{PH}(\mathbf{z}) \equiv \max_{f_d}\left\{Y(f_d), -\frac{1}{2T_r} \le f_d \le \frac{1}{2T_r}\right\}. \tag{16}$$

When the received radar returns are pure sea clutter, the feature PH takes small values; otherwise, the feature PH takes large values.

The position of the PH in the MNDAS is computed as follows:

$$f_d^{\max}(\mathbf{z}) = \arg\max_{f_d}\left\{Y(f_d), -\frac{1}{2T_r} \le f_d \le \frac{1}{2T_r}\right\}. \tag{17}$$

In addition, entropy can describe the confusion degree of systems or data [14]. Similarly, the MNDAS entropy can be used to determine whether the target exists. So, the third extracted feature, the VE of the MNDAS, is used to distinguish between sea clutter and returns with targets, and can be expressed as follows:

$$\text{VE}(\mathbf{x}) \equiv -\sum_{f_d} \tilde{Y}(f_d) \log \tilde{Y}(f_d),$$
$$\tilde{Y}(f_d) = \frac{Y(f_d)}{\sum_{f_d} Y(f_d)}. \tag{18}$$

The energy of sea clutter spreads over a wide range of Doppler frequency, and the MNDAS of sea clutter are more chaotic, so the sea clutter has the larger VE than the returns with targets.

Then, the third extracted feature, the LA, can be expressed as follows:

$$\text{LA}(\mathbf{z}) \equiv \sum_{f_d \in \Delta} Y(f_d),$$
$$\Delta = [f_d^{\max}(\mathbf{z}) - \delta_1, f_d^{\max}(\mathbf{z}) + \delta_2] \tag{19}$$

where Δ represents the maximal nonzero interval in which the $f_d^{\max}(\mathbf{z})$ is located. If received radar returns contain targets, the values of the feature LA are large; otherwise, the values are small.

To suppress sea clutter and make the detection performance of the detector insensitive to SCR, the MNDAS are suggested, and the three new features, PH, VE, and LA, are extracted from the MNDAS. Similar to the experiments in Fig. 3, the correlation coefficients between average SCRs and detection probabilities of the PH, VE, and LA are 0.521, 0.450, and 0.577, respectively. The detection capability of the feature RDPH is dependent on local SCR rather than average SCR. So, except the RDPH, the other nine features (three new Doppler features and six existing
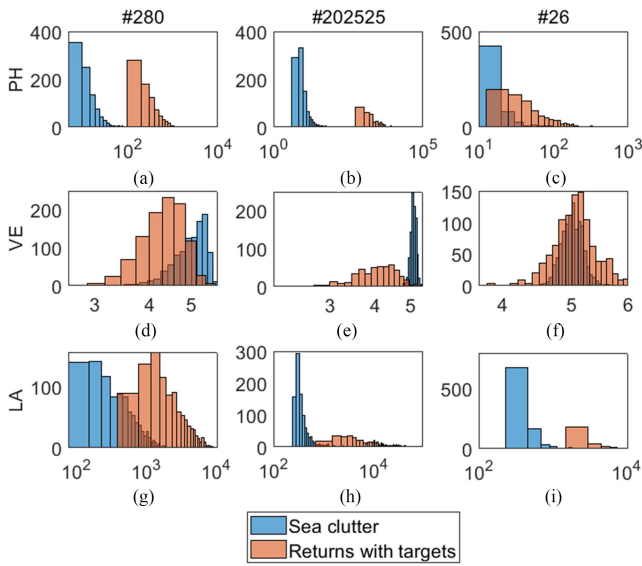
Fig. 5. Histogram comparisons of the three features between sea clutter and returns with targets on the three datasets from the IPIX database, where the horizontal axes use the logarithmic scale and $N = 512$.

features) can be divided into two categories, the ADHE, RAA, and RVE with correlation coefficients larger than 0.75 versus the RI, MS, NR, PH, VE, LA with correlation coefficients smaller than 0.67. It can be found that the sea clutter suppression does reduce performance dependence on SCR. In addition, based on the IPIX database [29], Fig. 5 compares of the three new features values between sea clutter and returns with targets, respectively. The overlapping extents of feature samples of sea clutter and returns with targets in histograms are different for the three datasets. The abilities of the three features to distinguish sea clutter and target returns are very different for different datasets and exhibit strong complementary. Therefore, their joint usage can improve detection performance and robustness.

C. Proposed Fast Feature-Based Detector

We extract the three new features from sea clutter, the PH, VE, and LA, to construct the training set $\mathbf{S}_H$ in the 3-D feature space. The rth feature sample of sea clutter is denoted as $\mathbf{z}_r = [z_{1,r}, z_{2,r}, z_{3,r}]$ in $\mathbf{S}_H$, $r = 12, \ldots, R$. The set $\mathbf{S}_H$ with R feature samples is expressed as follows:

$$\mathbf{S}_H = \begin{bmatrix} \mathbf{z}_1 \\ \mathbf{z}_2 \\ \vdots \\ \mathbf{z}_R \end{bmatrix} = \begin{bmatrix} z_{1,1}, z_{2,1}, z_{3,1} \\ z_{1,2}, z_{2,2}, z_{3,2} \\ \vdots \\ z_{1,R}, z_{2,R}, z_{3,R} \end{bmatrix}. \quad (20)$$

From the clutter-only training set $\mathbf{S}_H$ in 3-D feature space, the decision region Ω_H with a given false alarm rate P_f can be determined by the convexhull learning algorithm [14]. Fig. 6 demonstrates the convexhull learning process. Fig. 6(a) shows the two-class samples in the 3-D feature space. Fig. 6(b) plots the original convexhull of $\mathbf{S}_H$. Fig. 6(c) shows the optimal convexhull (decision region) with the desired false alarm rate, which is obtained by iteratively removing outliers from $\mathbf{S}_H$ and

the removed samples (false alarm points) are labeled by red stars. In the detection stage, it only needs to determine whether the test feature vector falls into the optimal convexhull. In this way, a new trifeature-based detector is built using the three new Doppler features from the MNDAS. More details on the convexhull learning algorithm refer to [14].

Owing to the clutter suppression ability of the MNDAS, the new trifeature-based detector can effectively detect small targets with very low SCRs and high velocity. When small targets have low velocity and high SCR, the detection capability of the new trifeature-based detector is not as good as the previous trifeature-based detector [14] because the previous trifeature-based detector describes the differences between two-class returns from both the time and Doppler domains. In contrast, the new trifeature-based detector only describes the differences from the Doppler domain. Thus, a dual trifeature-based detector strategy uses the low- and high-velocity trifeature-based detectors to detect the two classes of small targets, respectively. The previous trifeature-based detector [14] is used at the low-velocity tri-feature-based detector to find the first class of small targets, and the new trifeature-based detector is used at the high-velocity trifeature-based detector to detect the second class of small targets. The whole flowchart of the dual trifeature-based detector is shown in Fig. 7, where the training process uses the blue blocks, and the detection process uses the pink blocks.

In the training process, the same received sea clutter data are used as inputs for the low- and high-velocity trifeature-based detectors. Different feature extractors of the two trifeature-based detectors are used to extract individual features. As a result, $\mathbf{S}_H$ at the high-velocity trifeature-based detector and $\mathbf{S}_L$ at the low-velocity trifeature-based detector are obtained. The binary detection results of the two trifeature-based detectors are fused in the simple "or" rule. Or rather, the cell under test is declared to target presence if there is one trifeature-based detector to declare so. Due to simple "or" fusion, it is easy to control the false alarm rate of the final detection result. Let the desired false alarm rate be P_f. Then, the false alarm rate at each trifeature-based detector is set up at $0.5P_f$, which assures that the final false alarm rate is not more than P_f.

Even for low-velocity small targets, the fusion of the two trifeature-based detectors can improve detection performance, owing to the complementary of the two detectors. The two detectors are affected by the average SCR and Doppler separation of sea clutter and target returns. Fig. 8 shows the Doppler bandwidths and Doppler offsets of sea clutter and Doppler separations between sea clutter and target returns [37] on the eighty IPIX radar datasets, which illustrates the diversity of the Doppler offset and bandwidth of sea clutter. To analyze the influences of the ASCR and Doppler separation on each detector, Table II lists the correlation coefficients between the detection probabilities of each detector with the ASCR and Doppler separation. It can be seen that the major factor affecting the trifeature-based detector using the DAS is ASCR while the major factor affecting the trifeature-based detector using the MNDAS is Doppler separation. Thus, the two trifeature-based detectors are complementary in detection ability, which is the reason for the dual trifeature-based detection method to be developed and
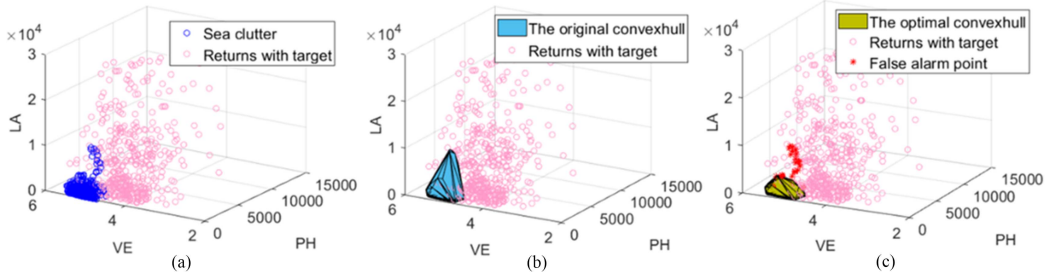
Fig. 6. (a) Feature vectors of sea clutter and returns with targets in the feature space, (b) the original convexhull of clutter, (c) the optimal convexhull of clutter.
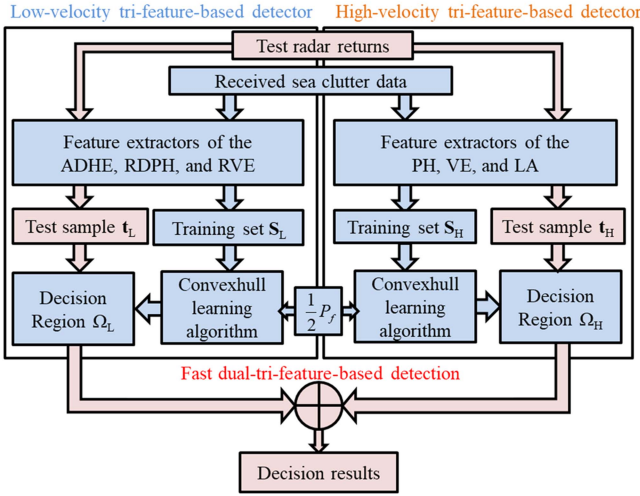

Fig. 7. Whole flowchart of the proposed fast dual trifeature-based detector.

TABLE II
CORRELATION COEFFICIENTS BETWEEN DETECTION PROBABILITY AND ASCR AND DOPPLER SEPARATION ON THE EIGHT IPIX DATASETS FOR EACH TRIFEATURE-BASED DETECTOR

Detectors	ASCR	Doppler separation
Low-velocity trifeature-based detector	0.7273	0.5867
High-velocity trifeature-based detector	0.5634	0.7343

for it to attain better detection results in the IPIX datasets than the trifeature-based detector using the DAS.

V. EXPERIMENTAL RESULTS AND ANALYSIS

To verify that different detectors or features are suitable for different types of returns with targets, the experiments are based on the four types of small targets, including the floating spherical block on the IPIX database in 1993, the floating small boats on the IPIX database in 1998, the motorized small boats on the CSIR database, and the UAV. On the ten IPIX radar datasets in 1993 [29], each dataset consists of complex returns time series of length 2^{17} (about 131 s) at 14 adjacent range cells. On the ten IPIX radar datasets in 1998, each dataset consists of complex returns of length 60000 (one minute) at about 28 adjacent range cells. Ten CSIR radar datasets [30] have different data sizes. Taking the dataset "TFA17-005" as an example, it consists of

complex returns time series of length 128160 (about 25 s) at 96 adjacent range cells. The UAV dataset consists of complex returns time series of length 1 200 000 (about 300 s) at 300 adjacent range cells.

A. Experiments on the IPIX and CSIR Radar Databases

This part mainly reports the experimental results on the IPIX and CSIR databases [29], [30]. Table III lists the average detection probabilities of the detectors on the IPIX database [29], where the false alarm rate is 0.001. For convenience in comparisons, the detectors are arranged by their average detection probabilities from low to high.

The detectors in Table III are divided into two groups according to the average detection probabilities. The first group includes the seven detectors with orange color in Table III that behave worse than the proposed detector, and the second group includes three detectors that behave better than the proposed detector. The performance of a feature-based detector is closely relevant to the underlying features and decision manners. Table IV lists the features and decision manners used in each detector. It is known that both the computation of features and the efficiency of decision determine the detection efficiency. The computational complexities of the NHE, ADHE, and RAA are $O(N)$, where N is the number of integrated pulses in the one decision [10], [12], [14]. The computational complexities of the RDPH and RVE are $O(N\log_2 N)$ by using the Fast Fourier transform (FFT) [14]. The features, RI, MS, and NR, require high computational complexities, and extracting the smoothed pseudo-Wigner–Ville distributions whose computational complexity is $O(NK\log_2 K)$, where K is the time window length [15]. Differently, the computational complexities of the proposed three Doppler features do not exceed $O(N\log_2 N)$, which is the reason for the proposed detector realizes the fast detection.

To quantitatively compare the detection efficiency, the CPU times of the nine detectors for the one decision on a personal computer are listed in Table V. The proposed detector attains the second shortest computational time, and it requires the double time of the trifeature-based detector and much shorter time than the other detectors. Moreover, it attains comparable performance with the TF-trifeature-based detector. A detector needs to consider both computational efficiency and detection performance. A synthetic index is introduced to assess a set of detectors. Let $(t_i, \bar{P}_i), i = 1, 2, \ldots, I$ be the CPU time for the
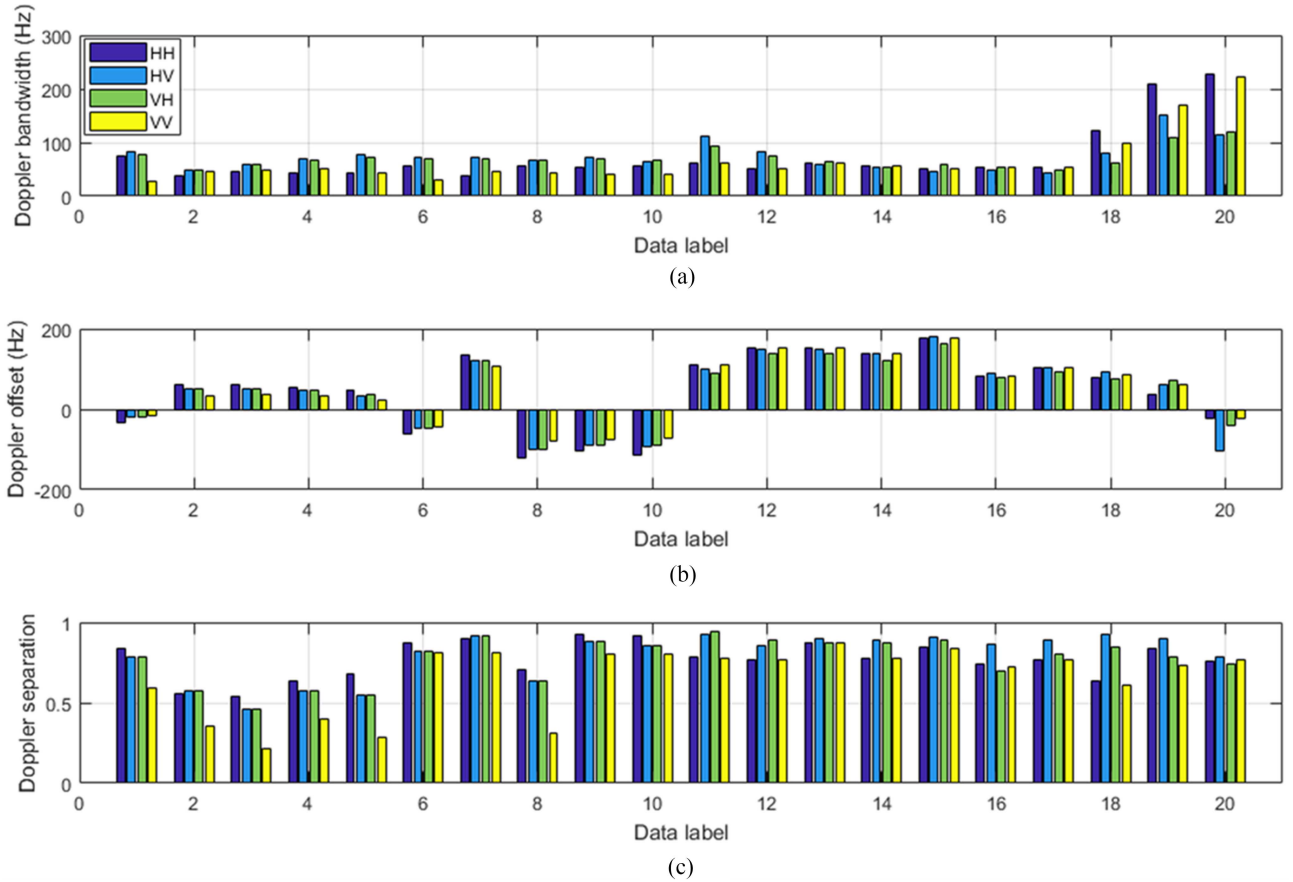
Fig. 8. Doppler bandwidths, Doppler offsets, and separations on the 80 IPIX radar datasets.

one decision and the average detection probability of the ith detector. Then, its synthetic index for comparison is given by

$$\beta(i) = \log_{10}\left(1 + \frac{\max_{i=1,2,\ldots,I}\{t_i\}}{t_i}\right) \times \frac{\max_{i=1,2,\ldots,I}\{1 - \bar{P}_i\}}{1 - \bar{P}_i} \tag{21}$$

where the logarithm in the first term is used to compress the too wide dynamic range. In terms of (21), a larger synthetic index means a better detector in the synthetic ability. Using the CPU times and the average detection probabilities of the nine detectors on the twenty datasets in the IPIX database when the false alarm rate is 10^{-3} and the integrated time is 0.512 s in Table III, the synthetic indexes of the nine detectors are calculated and listed in Table V. It can be seen that the proposed detector attains the largest synthetic index, owing to the fact that it obtains significant improvement in detection performance at the cost of small increase at CPU time for the one decision.

It is known that the detection performance is affected by target characteristics, including RCS and movement states. On the IPIX database, the test targets are floating small targets, which are often difficult to be distinguished from sea clutter in the Doppler domain. Differently, in the CSIR database, the test targets are moving small boats [30]. For moving small boats, their radar returns are easily distinguished from sea clutter in the Doppler domain, thus Doppler features are more effective

in detecting moving targets. To verify the performance of the proposed detector to the moving small targets, we use the ten datasets on the CSIR database to test the feature-based detectors. The average detection probabilities of the ten detectors are listed in Table VI. Among the ten detectors, the proposed detector is the third best in performance, and superior to the TF-trifeature-based detector.

Besides, the detection abilities at high sea states and low SCR cases are concerned in many applications. The ten CSIR datasets in Table VI are of the Douglas sea states not more than four. To examine the performance of detectors on high sea states, the CSIR datasets (TFC15-007 and TFC15-011) at five sea states are used, and their test targets are wave-rider rigid inflatable boats of the length of 5.7 m. The specific details of the datasets are listed in Table VII. The detection probabilities of the five detectors are listed in Table VIII, where the observation time for the one decision is 0.1 s and the false alarm rate is 0.001. At high sea states, strong sea clutter and abrupt RCS fluctuation of test targets often incur degradation in detection performance. The extent of degradation is dependent on detectors. It can be seen that the three out of the five detectors have quite different detection probabilities on the two datasets, and their detection abilities are not stable. The C-GLRT-LTD has comparable detection probabilities on the two datasets but is slightly poorer than the proposed detector. The proposed detector attains stable and best detection performance, owing to the dual trifeature-based

TABLE III
AVERAGE DETECTION PROBABILITIES OF THE ELEVEN DETECTORS ON THE IPIX DATABASE

Data for test	Detectors	Observation time	HH	HV	VH	VV	Average P_d
The twenty datasets of the IPIX radar database	SVM-based detector [16]	0.512 s	0.526	0.690	0.744	0.530	0.623
		1.024 s	0.517	0.732	0.757	0.505	0.628
	ADHE-based detector [12]	0.512 s	0.524	0.741	0.768	0.510	0.636
		1.024 s	0.614	0.822	0.831	0.590	0.714
	Trifeature-based detector [14]	0.512 s	0.577	0.736	0.776	0.569	0.665
		1.024 s	0.622	0.797	0.813	0.598	0.708
	Phase-feature-based detector [17]	0.512 s	0.633	0.786	0.801	0.626	0.712
		1.024 s	0.754	0.865	0.860	0.732	0.803
	PCA-based detector [24]	0.512 s	0.658	0.839	0.848	0.668	0.754
		1.024 s	0.748	0.874	0.876	0.735	0.808
	C-GLRT-LTD [37]	0.512 s	0.705	0.817	0.821	0.677	0.755
		1.024 s	0.770	0.857	0.856	0.739	0.806
	Proposed detector	0.512 s	**0.712**	**0.836**	**0.848**	**0.696**	**0.773**
		1.024 s	**0.781**	**0.889**	**0.887**	**0.769**	**0.832**
	TF-trifeature-based detector [15]	0.512 s	0.747	0.826	0.842	0.706	0.780
		1.024 s	0.821	0.882	0.877	0.789	0.842
	Feature compression-based detector [26]	0.512 s	0.807	0.880	0.888	0.788	0.841
		1.024 s	0.841	0.920	0.914	0.839	0.879
	KNN-based detector [27]	0.512 s	0.819	0.902	0.907	0.806	0.858
		1.024 s	0.884	0.936	0.931	0.868	0.905
#17(HH, HV) #54(HH, HV, VH, VV)	Graph-based detector [18]	0.512 s	-	-	-	-	0.643
	Proposed detector		-	-	-	-	**0.839**

The bold entities highlight the detection probabilities of the proposed method.

TABLE IV
FEATURE SPACE CONSTRUCTION AND DECISION MANNER OF THE DETECTORS

Detectors	Feature space construction	Decision manner
SVM-based detector [16]	NHE-RDPH-TIE	SVM decision
ADHE-based detector [12]	ADHE	Threshold decision
PCA-based detector [24]	RAA-RDPH-RVE-RI-MS-NR	
Graph-based detector [18]	Graph connectivity	
C-GLRT-LTD [37]	C-GLRT-LTD	
KNN-based detector [27]	NHE-RAA-RDPH-RVE-RI-MS-NR-GLRTLTD	Anomaly and threshold decision
Trifeature-based detector [14]	RAA-RDPH-RVE	Convexhull decision
Phase-feature-based detector [17]	NCZP-MPDF-DT	
TF-trifeature-based detector [15]	RI-MS-NR	
Feature compression-based detector [26]	NHE-RAA-RDPH-RVE-RI-MS-NR	
Proposed detector	PH-LA-VE ADHE-RDPH-RVE	

detector strategy and clutter suppression in the extraction of the Doppler features. Fig. 9 demonstrates the detection results of the five detectors on the dataset of TFC15-011. Fig. 9(a) shows the power map where the target trace is labeled by the red rectangle. At high sea states, the test target is sometimes shadowed by sea waves. An invisible target trace in the power map means low SCR, and the Doppler features without clutter suppression and amplitude/power features in the trifeature-based detector fail to find the target, which is probably the reason for its very low detection probability. Fig. 9(b)–(f) show the detection results of the five detectors, where the sporadic points in the subplots are false alarm points. Each detection result has 18 false

TABLE V
CPU TIMES OF THE ONE DECISION AND SYNTHETIC INDEXES OF THE NINE DETECTORS

Detectors	CPU time of one decision	Synthetic Index $\beta(i)$
Trifeature-based detector [14]	0.1066 ms	3.8203
Proposed detector	**0.2166 ms**	**5.1269**
Phase-feature-based detector [17]	12.3766 ms	1.7666
SVM-based detector [16]	23.8400 ms	1.0825
TF-trifeature-based detector [15]	89.0666 ms	1.0259
Feature-compression-based detector [26]	92.1236 ms	1.3936
PCA-based detector [24]	113.7301 ms	0.7997
C-GLRT-LTD [37]	146.0080 ms	0.6907
KNN-based detector [27]	264.4203 ms	0.7992

TABLE VI
AVERAGE DETECTION PROBABILITIES OF THE TEN DETECTORS ON THE CSIR DATABASE

Detectors	False alarm rate	Observation time	Average P_d
ADHE-based detector [12]	10^{-3}	0.1 s	0.305
	10^{-4}	0.2 s	0.167
Phase-feature-based detector [17]	10^{-3}	0.1 s	0.605
	10^{-4}	0.2 s	0.479
SVM-based detector [16]	10^{-3}	0.1 s	0.693
	10^{-4}	0.2 s	0.608
Trifeature-based detector [14]	10^{-3}	0.1 s	0.755
	10^{-4}	0.2 s	0.687
C-GLRT-LTD [37]	10^{-3}	0.1 s	0.758
	10^{-4}	0.2 s	0.566
PCA-based detector [24]	10^{-3}	0.1 s	0.878
	10^{-4}	0.2 s	0.765
TF-trifeature-based detector [15]	10^{-3}	0.1 s	0.897
	10^{-4}	0.2 s	0.855
Proposed detector	**10^{-3}**	0.1 s	**0.920**
	10^{-4}	0.2 s	**0.870**
Feature-compression-based detector [26]	10^{-3}	0.1 s	0.924
	10^{-4}	0.2 s	0.899
KNN-based detector [27]	10^{-3}	0.1 s	0.961
	10^{-4}	0.2 s	0.938

TABLE VII
PARAMETERS OF THE TWO CSIR DATASETS AT HIGH SEA STATE

File Name	TFC15-007	TFC15-011
Carrier frequency	9GHz (X-band)	9GHz (X-band)
Polarization	VV	VV
Range resolution	15 m	15 m
PRF	5000 Hz	5000 Hz
Significant wave height	2.23 m	3.16 m
Sea state	5	5
Target range cells	19th-21th	18th-20th

TABLE VIII
DETECTION PROBABILITIES OF FIVE FEATURE-BASED DETECTORS

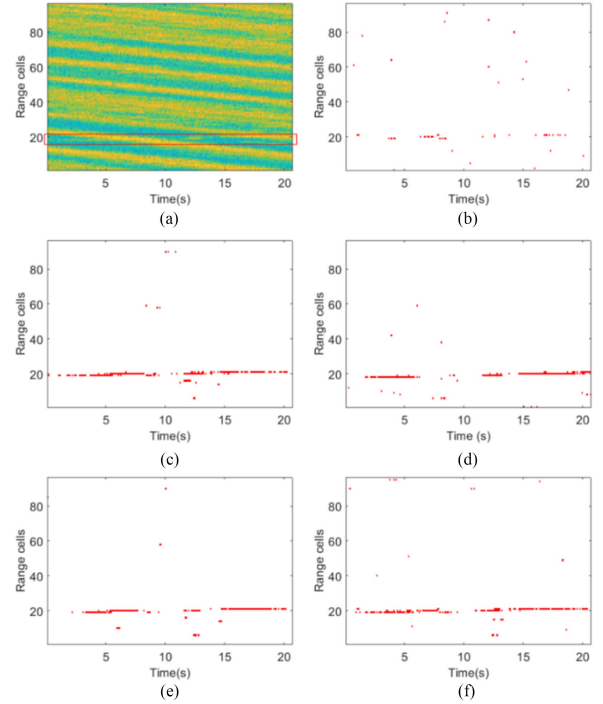| Dataset	TFC15-007	TFC15-011
Trifeature-based detector [14]	0.511	0.154
TF-trifeature-based detector [15]	0.354	0.683
C-GLRT-LTD [37]	0.579	0.559
PCA-based detector [24]	0.163	0.564
Proposed detector	**0.603**	**0.663**

Fig. 9. Detection results of the five detectors on the dataset of TFC15-011, (a) power map, (b) trifeature-based detector, (c) TF-trifeature-based detector, (d) C-GLRT-LTD, (e) PCA-based detector, (f) proposed detector.

alarm points which appear at different locations for individual detectors. Therefore, the proposed detector attains stable and good detection performance at high sea states.

B. Experimental Result on the UAV Dataset

In practical applications, maritime high-resolution radars need to detect both high-velocity low-altitude small targets and low-velocity/floating sea-surface small targets. To prove the ability of the proposed detector in this situation, we simulate a low-velocity small target and a high-velocity small target to add to the UAV dataset. In this way, the UAV dataset contains three different targets, a UAV and two simulated targets with adjustable SCR and radial velocity. The low-velocity simulated target has a variable SCR from –20to 10 dB and a variable radial velocity from –2 to 2 m/s. It locates on the left-bottom corner of the power map in Fig. 10, and its trace in the power map can be observed from the zoomed subfigure. The SCR and radial velocity curves with time are plotted in the two subfigures on the left-hand side of the power map. The high-velocity simulated target has a variable SCR from –20to 10 dB and a variable radial velocity from –10 to –7 m/s. It locates on the left-top corner of the power map in Fig. 10, and its trace in the power map can be observed from the zoomed subfigure. The SCR and radial velocity curves with time are plotted in the two subfigures on the right-hand side of the power map. The UAV under test in the dataset is a high-velocity small target of low SCR, its trace fails to be observed on the power map. The low-velocity simulated target appears at the 0th s and disappears at the 150th s. It moves toward the radar at 5.5 km first and then moves away from the
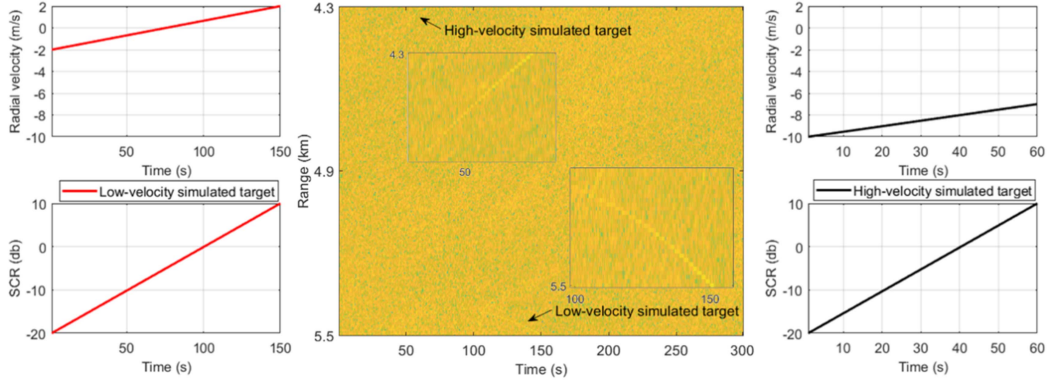
Fig. 10.   Power map of the UAV dataset with the UAV under test and two simulated low- and high-velocity targets and the SCR and radial velocity changes of the two simulated targets.
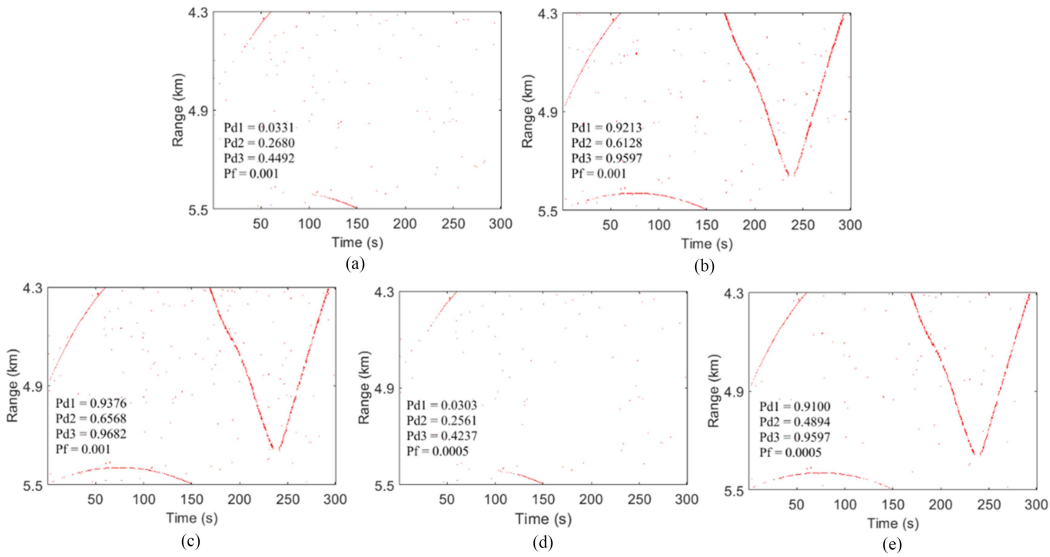

Fig. 11.   Detection result comparison of the three detectors on the UAV dataset: (a) The previous trifeature-based detector [14], (b) the TF-trifeature-based detector [15], (c) the proposed dual trifeature-based detector, (d) the low-velocity trifeature-based detector, and (e) the high-velocity trifeature-based detector.

radar at 5.4 km. The high-velocity simulated target appears at the 0th s and disappears at the 60th s.

The radar returns in the first 38 s, which is labeled as "Training region" in a rectangle box in Fig. 1(c), are used to train the convexhull decision regions of detectors at a given false alarm rate. The radar returns after the 38th s are used to detect and compute the detection probabilities. The false alarm rates of all three detectors are set up at 0.001, and the observation time of the one decision is 0.128 s. The detection results of the trifeature-based detector, the TF-trifeature-based detector, and the proposed detector are illustrated in Fig. 11, where "Pd1" is the detection probability of the UAV under test, "Pd2" is that of the low-velocity simulated target, "Pd3" is that of the high-velocity simulated target, and "Pf" is the false alarm rate in each subfigure. The detection results of the three detectors are all broken in the top of the "V"-shaped trace of the UAV, which is due to the radial velocity close to zero when the UAV turned back on the farthest point.

Because the RAA is invalid when SCR is very low and the RDPH is invalid when the Doppler peak of sea clutter is higher than that of target returns, the trifeature-based detector almost

fails to find the test UAV trace and part of the traces of the two simulated targets when their SCRs are low. When the two simulated targets are about to move out of the radar beam, their SCRs are high, and thus their traces can be detected. Thus, due to the inherent drawback of the features, the trifeature-based detector can work well only when SCR is enough regardless of target radial velocity. The extraction of the three TF features uses the clutter suppression in the time-Doppler domain by the normalized TFD [15], and thus it can effectively find both the UAV under test and the two simulated targets. However, the high computational complexities of the three TF features are conflictive with the fast detection sometimes. In the proposed detector, the dual trifeature-based detector fusion result, the results at the low-velocity trifeature-based detector and the high-velocity trifeature-based detector are demonstrated in Fig. 11(c)–(e). The low-velocity trifeature-based detector can effectively find the target trace as the SCR is high, and the high-velocity trifeature-based detector can effectively find high-velocity targets even though their SCRs are low, which is owing to the clutter suppression in the Doppler domain before the three new Doppler features are extracted in the high-velocity

trifeature-based detector. Eventually, the fusion of the two trifeature-based detectors can obtain significantly improved results.

VI. CONCLUSION

This article proposed a feature-based detector to realize the fast detection of low-velocity/floating small targets and low-altitude high-velocity small targets in the sea clutter background. In existing detectors, effective detection of the two classes of targets is often conflictive with fast detection. The proposed dual trifeature-based detector scheme fuses the result of the low-velocity trifeature-based detector and the high-velocity trifeature-based detector. The low-velocity trifeature-based detector uses an improved version of the trifeature-based detector to fast find low-velocity/floating small targets with higher SCRs. The high-velocity trifeature-based detector uses a new trifeature-based detector to fast find high-velocity small targets with very low SCR. The three Doppler features are extracted from the proposed MNDAS that contains adaptive clutter suppression, and thus they have the ability to find high-velocity small targets with very low SCR whose Doppler offsets fall outside the main clutter region of sea clutter. The effectiveness of the proposed dual trifeature-based detector is verified by the radar databases for small target detection in sea clutter.

REFERENCES

[1] K. D. Ward, R. J. A. Tough, and S. Watts, *Sea Clutter: Scattering, the K Distribution and Radar Performance*, 2nd ed. London, U.K.: IET, 2013, pp. 18–134.

[2] J. Guan, "Summary of marine radar target characteristics," *J. Radars*, vol. 9, no. 4, pp. 674–683, Aug. 2020.

[3] X. Cao, Y. Cheng, H. Wu, and H. Wang, "Nonstationary moving target detection in spiky sea clutter via time-frequency manifold," *IEEE Geosci. Remote Sens. Lett.*, vol. 19, 2022, Art. no. 3510505.

[4] M. Greco, P. Stinco, F. Gini, and M. Rangaswamy, "Impact of sea clutter nonstationarity on disturbance covariance matrix estimation and CFAR detector performance," *IEEE Trans. Aerosp. Electron. Syst.*, vol. 46, no. 3, pp. 1502–1513, Jul. 2010.

[5] K. J. Sangston, F. Gini, and M. V. Greco, "Coherent radar target detection in heavy-tailed compound-Gaussian clutter," *IEEE Trans. Aerosp. Electron. Syst.*, vol. 48, no. 1, pp. 64–77, Jan. 2012.

[6] P.-L. Shui and Y.-L. Shi, "Subband ANMF detection of moving targets in sea clutter," *IEEE Trans. Aerosp. Electron. Syst.*, vol. 48, no. 4, pp. 3578–3593, Oct. 2012.

[7] H. Leung, N. Dubash, and N. Xie, "Detection of small objects using a GA-RBF neural network," *IEEE Trans. Aerosp. Electron. Syst.*, vol. 38, no. 1, pp. 98–118, Jan. 2002.

[8] J. Hu, W. W. Tung, and J. B. Gao, "Detection of low observable targets within sea clutter by structure function based multifractal analysis," *IEEE Trans. Antennas Propag.*, vol. 54, no. 1, pp. 136–143, Jan. 2006.

[9] J. Guan et al., "Fractal characteristic in frequency domain for target detection within sea clutter," *IET Radar Sonar Navigation*, vol. 6, no. 5, pp. 293–306, Dec. 2012.

[10] D. C. Li and P. L. Shui, "Floating small target detection in sea clutter via normalized Hurst exponent," *Electron. Lett.*, vol. 50, no. 17, pp. 1240–1242, Aug. 2014.

[11] Y. F. Fan et al., "Weak target detection based on whole-scale Hurst exponent of autoregressive spectrum in sea clutter background," *Digit. Signal Process.*, vol. 101, no. 1, May 2020, Art. no. 102714.

[12] Z. X. Guo, P. L. Shui, and X. H. Bai, "Small target detection in sea clutter using all-dimensional Hurst exponents of complex time sequence," *Digit. Signal Process.*, vol. 101, no. 1, Mar. 2020, Art. no. 102707.

[13] Y. Shi, X. Xie, and D. Li, "Range distributed floating target detection in sea clutter via feature-based detector," *IEEE Trans. Geosci. Remote Sens. Lett.*, vol. 13, no. 12, pp. 1847–1850, Dec. 2016.

[14] P.-L. Shui, D.-C. Li, and S.-W. Xu, "Tri-feature-based detection of floating small targets in sea clutter," *IEEE Trans. Aerosp. Electron. Syst.*, vol. 50, no. 2, pp. 1416–1430, Apr. 2014.

[15] S.-N. Shi and P.-L. Shui, "Sea-surface floating small target detection by one-class classifier in time-frequency feature space," *IEEE Trans. Geosci. Remote Sens.*, vol. 56, no. 11, pp. 6395–6411, Nov. 2018.

[16] Y. Li, P. Xie, Z. Tang, T. Jiang, and P. Qi, "SVM-based sea-surface small target detection: A false-alarm-rate-controllable approach," *IEEE Geosci. Remote Sens. Lett.*, vol. 16, no. 8, pp. 1225–1229, Aug. 2019.

[17] J. Xie and X. Xu, "Phase-feature-based detection of small targets in sea clutter," *IEEE Geosci. Remote Sens. Lett.*, vol. 19, 2022, Art no. 3507405.

[18] K. Yan, Y. Bai, H.-C. Wu, and X. Zhang, "Robust target detection within sea clutter based on graphs," *IEEE Trans. Geosci. Remote Sens.*, vol. 57, no. 9, pp. 7093–7103, Sep. 2019.

[19] Y. L. Shi, T. T. Yao, and Y. X. Guo, "Floating small target detection based on graph connected density in sea clutter," *J. Electron. Inf. Technol.*, vol. 43, no. 11, pp. 3185–3192, Apr. 2021.

[20] S. Chen, F. Luo, and X. Luo, "Multiview feature-based sea surface small target detection in short observation time," *IEEE Geosci. Remote Sens. Lett.*, vol. 18, no. 7, pp. 1189–1193, Jul. 2021.

[21] X. Wu, H. Ding, N.-B. Liu, and J. Guan, "A method for detecting small targets in sea surface based on singular spectrum analysis," *IEEE Trans. Geosci. Remote Sens.*, vol. 60, 2022, Art. no. 5110817.

[22] J. Guan et al., "A method for detecting small slow targets in sea surface based on diagonal integrated bispectrum," *J. Electron. Inf. Technol.*, vol. 44, no. 7, pp. 2449–2460, Jul. 2022.

[23] Y. Fan, M. Tao, J. Su, and L. Wang, "Weak target detection based on joint fractal characteristics of autoregressive spectrum in sea clutter background," *IEEE Geosci. Remote Sens. Lett.*, vol. 16, no. 12, pp. 1824–1828, Dec. 2019.

[24] T. Gu, "Detection of small floating targets on the sea surface based on multi-features and principal component analysis," *IEEE Geosci. Remote Sens. Lett.*, vol. 17, no. 5, pp. 809–813, May 2020.

[25] H. K. Zhou and T. Jiang, "Decision tree based sea-surface wake target detection with false alarm rate controllable," *IEEE Signal Process. Lett.*, vol. 26, no. 6, pp. 793–797, Jun. 2019.

[26] P. Shui, Z. Guo, and S. Shi, "Feature-compression-based detection of sea-surface small targets," *IEEE Access*, vol. 8, pp. 8371–8385, 2020.

[27] Z.-X. Guo and P.-L. Shui, "Anomaly-based sea-surface small target detection using K-nearest-neighbor classification," *IEEE Trans. Aerosp. Electron. Syst.*, vol. 56, no. 6, pp. 4947–4964, Dec. 2020.

[28] X. Chen, N. Su, Y. Huang, and J. Guan, "False-alarm-controllable radar detection for marine target based on multi features fusion via CNNs," *IEEE Sensors J.*, vol. 21, no. 7, pp. 9099–9111, Apr. 2021.

[29] Cognitive Systems Laboratory, McMaster University, Canada, The IPIX radar database[OL]. Accessed: Oct. 11, 2012. [Online]. Available:http://soma.mcmaster.ca//ipix.php

[30] The Defence, Peace, Safety, and Security Unit of the Council for Scientific and Industrial Research, The Fynmeet radar database[OL]. Accessed: Dec. 13, 2018. [Online]. Available:http://www.csir.co.ca/small_boat_detection

[31] M. I. Skolnik, *Introduction to Radar Systems*, 3rd ed. New York, NY, USA: McGraw-Hill, 2014, pp. 141–148, Chap. 3, Section 3.6.

[32] X. Chen, J. Guan, Z. Bao, and Y. He, "Detection and extraction of target with micromotion in spiky sea clutter via short-time fractional fourier transform," *IEEE Trans. Geosci. Remote Sens.*, vol. 52, no. 2, pp. 1002–1018, Feb. 2014.

[33] J. Carretero-Moya et al., "Application of the radon transform to detect small-targets in sea clutter," *IET Radar Sonar Navigation*, vol. 3, no. 2, pp. 155–166, Oct. 2009.

[34] H. Y. Fan, Y. M. Jiang, and G. Y. Kuang, "Target detection in non-stationary clutter background and Riemannian geometry," *IET Radar Sonar Navigation*, vol. 8, no. 4, pp. 376–381, Jul. 2014.

[35] D. C. Li and P. L. Shui, "Floating small target detection in sea clutter via normalized Doppler power spectrum," *IET Radar Sonar Navigation*, vol. 10, no. 4, pp. 699–706, Nov. 2016.

[36] G. Weinberg and A. Alexopoulos, "Analysis of a dual order statistic constant false alarm rate detector," *IEEE Trans. Aerosp. Electron. Syst.*, vol. 52, no. 5, pp. 2567–2574, Oct. 2016.

[37] S. N. Shi and P. L. Shui, "Detection of low-velocity and floating small targets in sea clutter via income-reference particle filters," *Signal Process.*, vol. 148, no. 1, pp. 78–90, Feb. 2018.

Zi-Xun Guo was born in Xi'an, Shaanxi, China, in 1994. She received the B.S. degree in intelligent science and technology and the Ph.D. degree in signal processing from the National Laboratory of Radar Signal Processing, Xidian University, Xi'an, China, in 2016 and 2022, respectively.

She is currently a Postdoctoral Fellow with Northwestern Polytechnical University, Xi'an, China. Her research interests include sea clutter, signal processing, radar target detection, and machine learning.

Xiao-Hui Bai was born in Baoji, Shaanxi, China, in 1998. She received the B.S. degree in electrical engineering in 2018 from Xidian University, Xi'an, China, where she is currently working toward the Ph.D. degree in signal and information processing with the National Laboratory of Radar Signal Processing.

Her research interests include radar target detection and machine learning.

Peng-Lang Shui (Senior Member, IEEE) received the M.S. degree in mathematics from Nanjing University, Nanjing, China, and the Ph.D. degree in electrical engineering from Xidian University, Xi'an, China, in 1992 and 1999, respectively.

He is currently a Professor with the National Laboratory of Radar Signal Processing, Xidian University. His research interests include sea clutter modeling and analysis, radar target detection, and image processing.

Ling Wang received the B.Sc., M.Sc., and Ph.D. degrees in electronic engineering from Xidian University, Xi'an, China, in 1999, 2002, and 2004, respectively.

From 2004 to 2007, he worked with Siemens and Nokia Siemens Networks. Since 2007, he has been with the School of Electronic and Information, Northwestern Polytechnical University, Xi'an, China, and was promoted to Professor in 2012. His current research interests include array processing and smart antennas, wideband communications, cognitive radio, adaptive antijamming for satellite communications, satellite navigation, and date link systems.

Jia Su (Member, IEEE) received the B. Eng. degree in communication engineering and the M. Eng. degree in optical communication from the Guilin University of Electronic Technology, Guilin, China, in 2008 and 2011, respectively, and the Ph.D. degree in signal and information processing from Xidian University, Xi'an, China, in 2015.

He is currently an Associate Professor with Northwestern Polytechnical University (NPU), Xi'an. His research interests include radar signal processing and time frequency analysis.